Numerical investigation of the two-dimensional gas temperature distribution based on tunable diode laser absorption spectroscopy

JIE SHAO[*], LIMING WANG, CHAOFU YING

Institute of Information Optics, Zhejiang Normal University, Jinhua 321004, PR China

[*]Corresponding author: shaojie@zjnu.cn

Based on tunable diode laser absorption spectroscopy and modified adaptive algebraic reconstruction technique, two-dimensional tomographic reconstruction was derived for the gas temperature distribution in the range of 600–1400 K in the controlled projections. It is explicitly shown that the quality of temperature reconstruction is heavily dependent on the relative sensitivity of the selected spectrum and the algorithm of modified adaptive algebraic reconstruction technique but independent of the complexity of the present field distribution. When the relative sensitivity is less than 1.5, the accuracy of reconstruction relates to the relative sensitivity of the selected spectrum and improves with the increase in relative sensitivity. When the relative sensitivity is larger than 1.5, the accuracy is mainly limited by the algorithm of modified adaptive algebraic reconstruction technique.

Keywords: tomographic, modified adaptive algebraic reconstruction technique (MAART), tunable diode laser absorption spectroscopy (TDLAS).

1. Introduction

Tunable diode laser absorption spectroscopy (TDLAS) was known as a method of choice for *in situ* measurements of combustion parameters (*i.e.*, temperature, concentration, flux) in the industrial environment, with advantages of quick response, high precision, non-intrusive detection, and simple operation [1–5]. For combustion diagnosis, the measurements of temperature and concentration distribution are more important for optimizing the combustion efficiency and reducing the pollution emissions. Unfortunately, the traditional line-of-sight (LOS) TDLAS technique still cannot fulfill the increasing demand in rapid and accurate measurements of the concentration and temperature distribution in the combustion diagnostics [6].

The recent research combining TDLAS with computer tomography (CT) determines the temperature distribution of a specific chemical species for fluid mechanics and combustion applications [7–10]. The conventional medical CT technique requires numerous projections to cover the entire probed object at many traversing locations and orientations. However, in practical combustion applications, the number of projections is limited by the dynamic characteristics of the flow field and the space available for fiber-optic access, which results in typically under sampled limited tomographic data [8]. With the development of the TDLAS and the potential to leverage reconstruction algorithms from CT technique, the reconstruction technique of temperature and concentration have been studied by many researchers in recent years. For instance, a design criterion was presented by TERZIJA *et al.* for the optimal beam geometry for imaging performance and results in an irregular array with only 27 measurement paths through the subject for their application to an engine cylinder, and a demonstration measurement of propane plumes in air illustrated the fidelity of this optimization [11]. Hyperspectral absorption spectroscopy was applied by LIN MA *et al.* to reduce the number of rays, and simulated annealing algorithm was adopted in the calculation in the 2D reconstruction of temperature [12–14]. JUNLING SONG got temperature and concentration distributions for an optical path by scanning multiple absorption lines of H_2O, and took a virtual ray method to improve spatial resolution [15]. WANG *et al.* developed a tunable diode laser absorption tomography system which was capable of acquiring NH_3 concentration and temperature distributions by four optical sources and detectors mounted on rotational stages in about 100 ms using four cylindrical retroreflectors [6].

As alluded to above, almost all researchers focus on either how to obtain steady and effective distribution by finite measured data, or how to improve the optical design and tomography image quality. As a crucial step in the sensor design, the selection of spectrum is apparently related to the precision of temperature reconstruction. There are already some past works in the area of the selection of absorption transitions for non-uniform temperature measurement fields [16–19]. However, the impacts of the selection of the spectrum on the temperature reconstruction have been seldom studied. In this paper, we combined the TDLAS technique with modified adaptive algebraic reconstruction technique (MAART) to obtain tomographic images of temperature from the incomplete system of projections as References [6, 15, 20] described. This method provides better reconstruction with fast computation and high quality. In this study, the methods of temperature reconstruction were discussed and evaluated from the numerical simulation, and ten different selected spectra of H_2O were expanded to examine the relationship between the relative temperature sensitivity of the selected spectrum and the accuracy of temperature reconstruction. The results have shown that the accuracy of reconstruction could be improved by selecting the spectrum which has higher overall level of relative sensitivity, and there exists a critical corner value in a similar L-shaped curve in the relationship between the relative temperature sensitivity and the average of error reconstruction.

2. Methodology

2.1. Optical absorption fundamentals

According to the Beer–Lambert law

$$\frac{I(v)}{I_0(v)} = \exp[-PXS_i(T)\Phi_i L] \tag{1}$$

the ratio of the transmitted laser intensities $I(v)$ and the incident laser intensity $I_0(v)$ of laser radiation that passes through an absorbing medium at a particular frequency v is exponentially changing with the total pressure P [atm], the path length L [cm], the mole fraction of the absorbing species X_j, the temperature-dependent line strength $S_i(T)$ [cm^{-2}atm^{-1}] and the area normalized line-shape Φ_i [cm].

The temperature-dependent line strength is given by

$$S(T) = S(T_0)\frac{Q(T_0)}{Q(T)}\frac{T_0}{T}\exp\left[-\frac{hcE''}{k}\left(\frac{1}{T}-\frac{1}{T_0}\right)\right]\frac{1-\exp\left(-\frac{hcv_0}{kT}\right)}{1-\exp\left(-\frac{hcv_0}{kT_0}\right)} \tag{2}$$

where $S(T_0)$ is the line strength at a reference temperature T_0, $Q(T)$ is the molecular partition function, h [Js] is Planck's constant, c [cm/s] is the speed of light, k [J/K] is Boltzmann's constant, E'' [cm^{-1}] is the lower-state energy, and v_0 [cm^{-1}] is the line center frequency of the transition [21].

The temperature can be inferred from the measured ratio of integrated absorbance for two different temperature-dependent transitions from the same species. Because the two integrated absorbances are obtained with the same partial pressure and path length, the ratio of these two integrals easily reduces to the ratio of line strengths according the Eqs. (1) and (2),

$$R(T) = \frac{A_1}{A_2} = \frac{\int PLXS_1(T)\Phi_{v_1}\,dv}{\int PLXS_2(T)\Phi_{v_2}\,dv} = \frac{S_1(T)}{S_2(T)} =$$

$$= \frac{S_1(T_0)}{S_2(T_0)}\exp\left[-\frac{hc}{k}(E_2''-E_1'')\left(\frac{1}{T}-\frac{1}{T_0}\right)\right] \tag{3}$$

According Eqs. (2) and (3), the gas temperature could be deduced by two transition lines with dissimilar energy

$$T = \frac{\frac{hc}{k}(E_2''-E_1'')}{\ln[R(T)]+\ln[R(T_0)]+\frac{hc}{k}\frac{(E_2''-E_1'')}{T_0}} \tag{4}$$

It is moreover customary to define an absolute temperature sensitivity as dR/dT and a relative one as $(dR/R)/(dT/T)$, which can be deduced from Eq. (4) as Ref. [22] described:

$$\frac{dR}{dT} = \frac{hc}{k}(E_2'' - E_1'')\frac{1}{T^2}\frac{S_1(T_0)}{S_2(T_0)}\exp\left[-\frac{hc}{k}(E_2'' - E_1'')\left(\frac{1}{T} - \frac{1}{T_0}\right)\right] \quad (5)$$

$$\frac{dR/R}{dT/T} \approx \frac{hc}{k}\frac{(E_2'' - E_1'')}{T} = 1.438\frac{(E_2'' - E_1'')}{T} = 1.438\frac{\Delta E''}{T} \quad (6)$$

The two lines should have sufficiently different lower state energy E'' to yield an adequate signal-to-noise ratio that is sensitive to the probed temperature. Therefore, at a specific temperature the sensitivity increases with dissimilar energy E'' increasing.

2.2. Tomography algorithm

A LOS measurement is performed along the ray, and the integrated absorbance across a transition can be written as a discretization expression

$$A_{\upsilon, i} = \sum_{j=1}^{N} [PS(T)X]_{\upsilon, j}L_{i,j} = \sum_{j=1}^{N} f_{\upsilon, j}L_{i,j} \quad (7)$$

where i is the index of the ray, N is the total number of grid points ($j = 1, 2, …, N$, $N = n^2$), $A_{\upsilon, i}$ denotes the integrated absorbance across the transition at the wavelength υ. The absorption coefficient $f_{\upsilon, j}$ containing the parameters of line strength $S_{\upsilon, j}(T)$, gas molar fraction of absorbing species X, and total pressure of P, was calculated in all the grids according to the tomography algorithm at two independent wavelengths to infer the unknown temperature and concentration of the gas [15]; $L_{i,j}$ is the length that the ray i crosses to span the grid point j. But this length is only relevant with the angle and the position. When the total number of rays is M for projection, the Eq. (7) can be given by:

$$\begin{aligned}
L_{11}f_1 + L_{12}f_2 + … + L_{1N}f_N &= A_1 \\
L_{21}f_1 + L_{22}f_2 + … + L_{2N}f_N &= A_2 \\
… \\
L_{M1}f_1 + L_{M2}f_2 + … + L_{MN}f_N &= A_M
\end{aligned} \quad (8)$$

where the subscript υ in the Eq. (7) has been omitted in Eq. (8) and the following Eq. (9) and Eq. (10). The application of the algebraic reconstruction technique (ART) solves the linear equation sets of Eq. (8) in the iterative Eqs. (9) and (10):

$$\mathbf{f}^{(k)} = \mathbf{f}^{(k+1)} + \alpha\frac{A_i - \mathbf{L}_i \cdot \mathbf{f}^{(k-1)}}{\mathbf{L}_i \cdot \mathbf{L}_i}\mathbf{L}_i = \mathbf{f}^{(k+1)} + \alpha^k(A_i - \mathbf{L}_i \cdot \mathbf{f}^{(k-1)}) \quad (9)$$

$$\alpha_j^k = \beta \times \frac{f_j^{k-1} L_{ij}}{\sum\limits_{j=1}^{N} f_j^{k-1} L_{ij}} \tag{10}$$

where k is the iteration index in the program, α is the relaxation parameter, A_i is the projection, and the subscript i represents the beam ($i = 1, 2, …, M$), β is a constant. In this paper, we select β during the procedure of the calculation complying with the guidelines in [20]. Iteration index k increases when calculation is performed through all projections [15]. Unlike the ART method [23], the relaxation parameter in the MAART method is automatically changed during the reconstruction procedure, as shown in Eq. (10). From the Eq. (10), we can find that the larger contribution of absorption to the ray integral, the larger an adjustment step during the iteration.

In this paper, we use the MAART method just as WANG *et al.* and JUNLING SONG did [6, 15]. They had used this algorithm for tomography reconstruction and had already achieved a great agreement between the phantom and reconstruction. We only apply the horizontal and vertical directions [8], the iterative sequence is applied in horizontal and vertical iteration alternately. This process repeats until the results meet the convergence condition. First initial concentration and temperature distributions are assumed, and the MAART method for the first wavelength of the line pair v_1 is applied to obtain f_{v1}. This process is then repeated for the second wavelength of the line pair v_2 to obtain f_{v2}. Utilizing the ratio of the f_{v1} and f_{v2} and then using the Eq. (4), we can obtain the distribution of temperature.

3. Simulation

To evaluate the fidelity of the reconstructions from the TDLAS tomography system, numerical simulation was carried out for an assumed distribution of a (10×10) cm square plane. In this example, we used a total of 20 projection locations (10 horizontal and 10 vertical, 10 beams were aligned in the x direction and 10 in the y direction, respectively) and divided the interest zone into 100 squares of the same size, so the dimension of the grid was 10×10 ($n = 10$, $N = 100$). As for the selection of the grid we considered two points: one is that the accuracy of the reconstruction using ART algorithm changes little with the increasing number of variables (grid dimension) when the statistic error in the whole measurement region is considered; second is that the time-consumption of reconstruction seriously increases with the densities of the grids. About the essence of the ART decide these two points [23–25]. Therefore we select the 10×10 as an example to study. A spatial resolution of 1 cm for both X and Y axis directions would be obtained. The total pressure was kept in 1 atm. In order to study the influence of different spectra on the reconstruction of temperature, we assumed that the concentration was constant through the whole program of reconstruction. A symmetric temperature distribution model was created by superimposing Gaussian peaks on a paraboloid (unimodal distribution) to simulate a representative multi-modal and
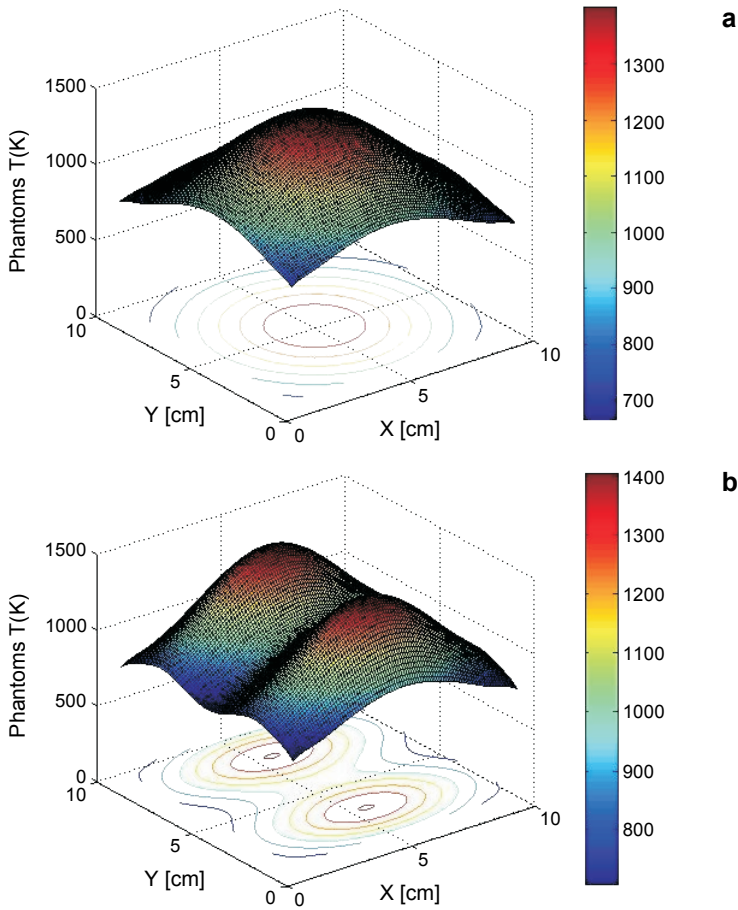
Fig. 1. The assumption model of temperature: unimodal phantom (**a**), and bimodal phantom (**b**).

the symmetric temperature distribution probably encountered in practical combustion devices at the 600–1400 K temperature range, as depicted in Fig. 1**a**. The temperature at the location of peak (5, 5) of this distribution is 1400 K. For confirming the exactness of the algorithm and lack of the loss of generality, another temperature distribution model in which two Gaussian peaks on a paraboloid (bimodal distribution) at the same temperature range was also used to simulate the reconstruction of temperature as shown in Fig. 1**b**. Some research has been conducted to reconstruct the temperature distribution in the experiment in the References [11, 15, 26] but just the temperature range is different. Some researchers have used these analogous phantoms to simulate the gas distributions in the References [20, 27]. So in this paper, we select these two distributions as the temperature distribution as shown in Fig. 1. The location of peak (3, 5), (8, 5) at the bimodal distribution has the same temperature, 1397 K. In addition, these models were smoothed by the method of natural bi-cubic spline interpolation which

was introduced in the Reference [28]. Thus high resolution images were obtained. A two-dimensional contour graph of the three-dimensional phantom distribution is displayed at the bottom of the picture in Fig. 1. Water was one of attractive combustion species to be monitored for a combustion diagnosis due to the relative abundance of water vapor as a combustion by-product and the widespread absorption transitions. Computations were performed to numerically simulate the performance of tomography algorithm for retrieving the temperature distributions using these two phantom distributions of H_2O from the combustion described above.

4. Reconstruction process and evaluation

Firstly, we select the spectra of H_2O around 1394.65 nm corresponding to the two peaks at 7169.8 and 7170.3 cm^{-1}, respectively. Figure 2 shows the calculated candidate H_2O spectra (at pressure 1 atm, 3.2% H_2O in N_2, L is 10 cm) based on HITEMP database at the temperature of 1000 K. In practice, there are more than 10 transitions in the range of this spectrum, as shown in Fig. 2. However, there are two apparent ab-
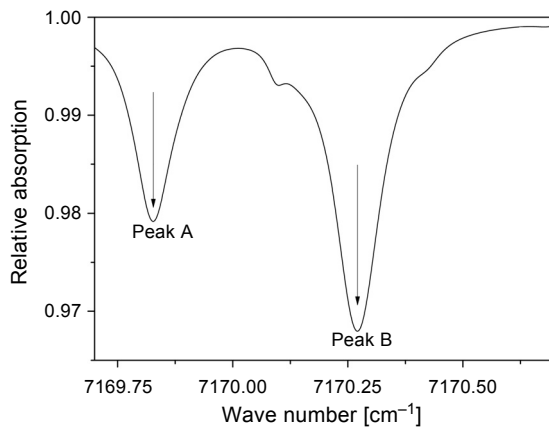

Fig. 2. The simulated spectra at the temperature of 1000 K for the H_2O transition near 1394.65 nm.

sorption peaks in the structure which are peak A and peak B with lower state energy 2400 and 419 cm^{-1}, respectively. The absorption of two peaks is great enough to meet detectability of direct absorption spectroscopy for a single-diode-laser sensor system for real-time measurements of temperature. The line strength of peak A and peak B is 3.25×10^{-3} and 5.79×10^{-3} cm^{-2}/atm at 1000 K, respectively, and the line strengths are calculated by the Eq. (2) in the temperature range of interest from 600–1400 K, which is shown in Fig. 3. Meanwhile, the ratio of the two line strengths is also shown in Fig. 3 which is calculated from Eq.(3).

The results show that the ratio is a strictly monotonically increasing function as the temperature increases, so the temperature can be measured using the selected spec-
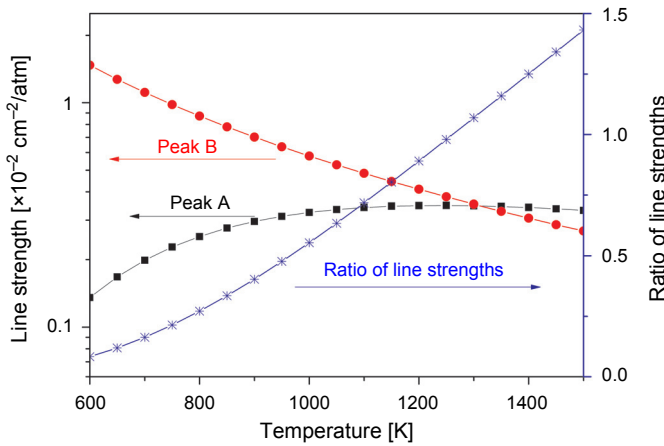
Fig. 3. Line strength as a function of temperature. Temperature is inferred from the ratio of line strengths for peak A and peak B.
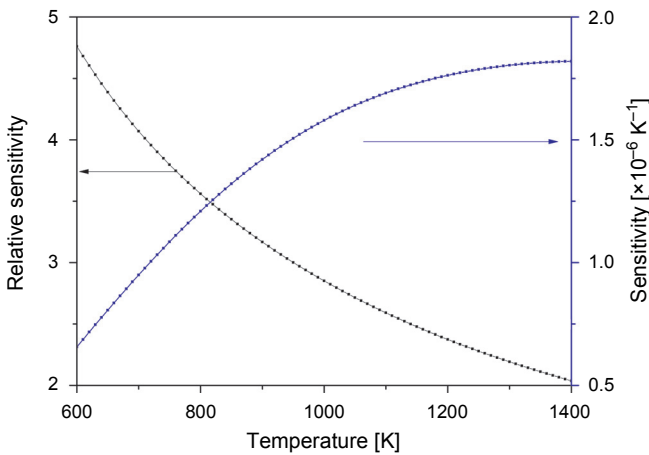

Fig. 4. The sensitivity and relative sensitivity as a function of temperature near 1394.65 nm.

tra in the temperature range of interest. For more information, the sensitivity and the relative sensitivity are shown in Fig. 4. From this figure, we can see that the relative sensitivity is at the range of 2 to 5, and the relative sensitivity at low temperature is larger than that at high temperature, which means that there is higher accuracy at low temperature using this selected spectrum as a temperature sensor.

Combining the MAART with TDLAS technique, the temperature reconstruction was performed to obtain images of temperature distribution of a (10×10) cm square plane of this selected line pair. The Figure 5**a** and 5**b**, respectively, displays the reconstructed temperature distribution of each pixel at the unimodal and bimodal pattern. Besides, these results also use the natural bi-cubic spline interpolation to obtain a smoothed and high spatial resolution image. It can be seen from the bottom of Fig. 5
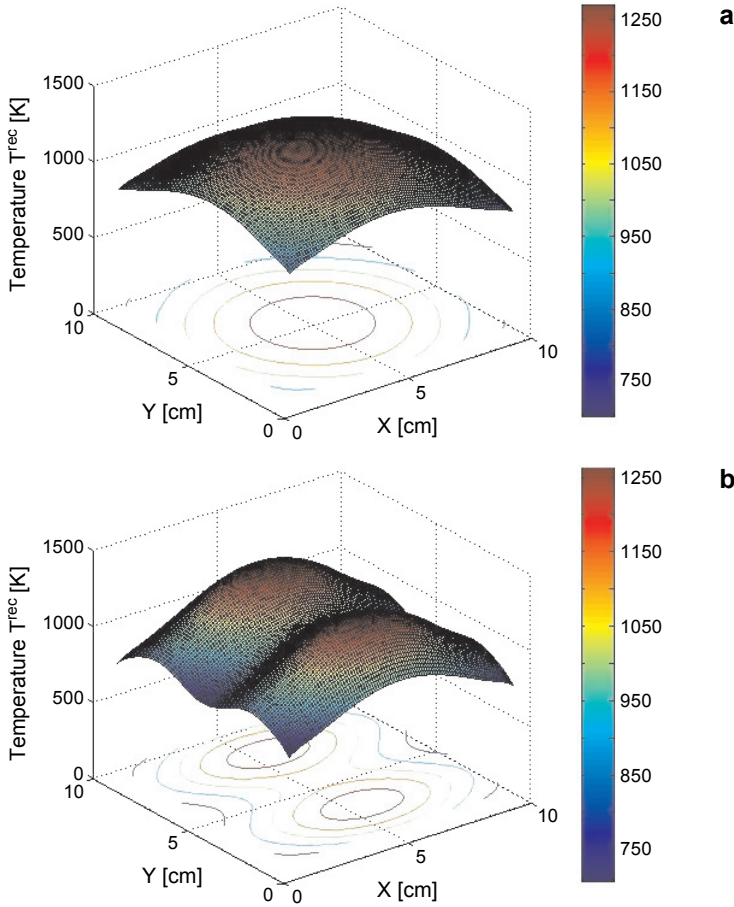
Fig. 5. Temperature reconstruction of each grid: unimodal distribution (**a**), and bimodal distribution (**b**).

that the two-dimensional contour graph of the temperature reconstruction distribution has some resemblance with the contour graph of the assumed model in Fig. 1. From the results of reconstruction, the peaks of temperature locate at the pixels (3, 5) and (8, 5) in the bimodal distribution, and locate at the pixel (5, 5) in the unimodal distribution, which are exactly the same as the assumption model. The temperatures of these peaks are 1253, 1253 and 1270 K, respectively, corresponding to 1393, 1393 and 1400 K in the assumption model. Comparing the reconstruction with the phantom, the least absolute error of temperature is only 0.0698 K located at the grid of (1, 10) in the unimodal distribution, and 1.064 K located at the grid of (3, 9) and (9, 3) of the bimodal distribution, respectively.

To quantify the quality of the reconstructed temperature, we define the relative error of each grid and normalized average error as $e_{T, l, s}$ and e_{ave} which also can be seen from [29]:

$$e_{T,l,s} = \frac{\left| T^{\text{rec}}_{l,s} - T_{l,s} \right|}{\left| T_{l,s} \right|} \tag{11}$$

$$e_{\text{ave}} = \frac{\sum_{l=1}^{n} \sum_{s=1}^{n} \frac{\left| T^{\text{rec}}_{l,s} - T_{l,s} \right|}{\left| T_{l,s} \right|}}{n \times n} \tag{12}$$

where $T^{\text{rec}}_{l,s}$ and $T_{l,s}$ represent the temperature in reconstruction distribution and assumed distribution for the grid (l, s) separately. The subscript l and s represent the pixel point number. These two quantities, the relative pixels error $e_{T,l,s}$ and the average error eave, provide a criteria for measured deviation $T^{\text{rec}}_{l,s}$ of to the phantoms.

Using the above criteria, the relative errors $e_{T,l,s}$ are about 2%–10% in the bimodal model, and 2%~9% in the unimodal model, which are calculated by the Eq. (11) and
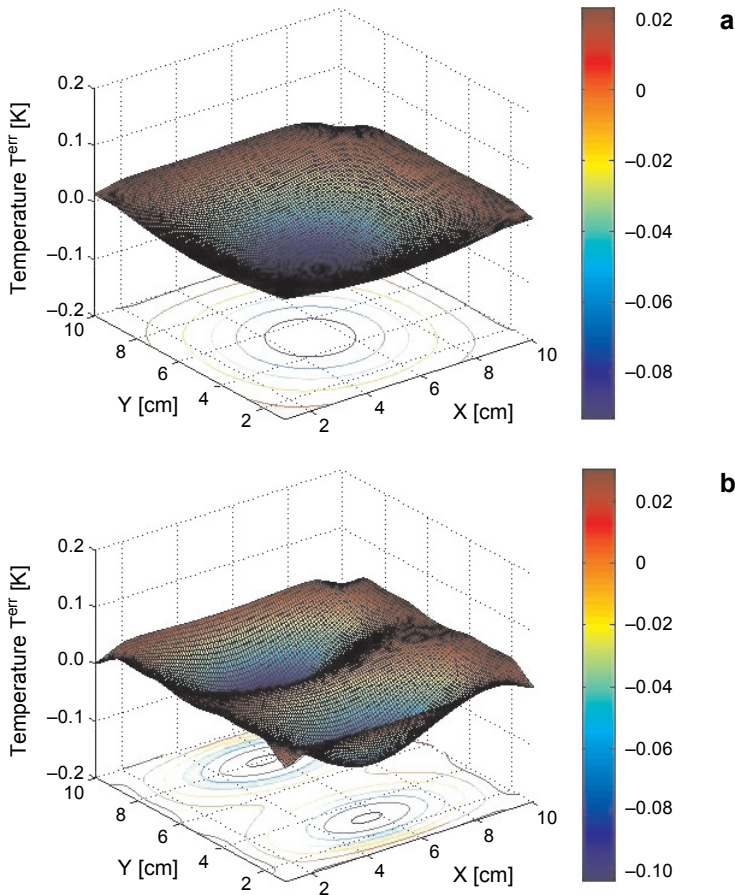

Fig. 6. The relative error of each grid in temperature reconstruction: unimodal distribution (**a**), and bimodal distribution (**b**).

shown in Fig. 6. Apparently, the extreme relative reconstruction error $e_{T, l, s}$ of these two phantoms occurs at the peak location and the adjacent grids as shown in Fig. 6. As mentioned previously, the phantoms are created by superimposing Gaussian peaks on a paraboloid to simulate practical distributions, and, therefore, have a gradient on the peak location grids. This also indicates that the peak of the reconstruction would be smoothened by the algorithm with a correction of values in the neighboring grids. Furthermore, the smaller error occurs at the edge and corner grids in both unimodal and bimodal model compared with the peak location grids and the overall reconstruction error is significantly smaller. So we then use the average error eave to quantify the lever of the overall error. The corresponding average error eave is 2.9% in the bimodal model, 2.7% in the unimodal can be calculated by the Eq. (12) obtained from the relative reconstructed error. Although the total projections of 20 for each wavelength are much lower than the number of unknown variables (100 grids of temperature and concentration), the appearance and location of peaks in both bimodal and unimodal distribution in the reconstructions are excellently identical with the models.

As the result illustrated above, the validity and feasibility of this method are verified by MAART and LOS system. The system based on the LOS absorption spectroscopy from two orthogonal projection directions can get the higher temporal resolution in practice. The time of the whole program of reconstruction is satisfactory in a few seconds. This method and simulation program have the feasibility and practicality for the implementation of temperature distribution reconstruction in practice both in the precision and speed.

5. Results and analysis

Although the results of temperature reconstruction are satisfactory using MAART with TDLAS techniques, the deviation still exists between the results and anticipation. The reconstructions of several kinds of spectra structure are realized to understand the cause of deviation from the phantom in this study.

We selected ten different absorption line-pairs of spectra for the temperature reconstructions, and the detailed information of ten line-pairs candidates is shown in Table 1. Since the value of the relative sensitivity is not a constant value in the 600–1400 K temperature range, the average relative sensitivity is used as a criterion to evaluate the whole level of relative sensitivity of the selected spectrum in this temperature range. The reconstruction results of the line pair 1 in Table 1 have been discussed above. The lack of space forbids the displacement of the reconstruction results of each grid of other nine candidate line pairs in Table 1, but other nine line pairs are all individual line pairs which are also used in the study of the influence of different sensitivity to the temperature reconstructions. The average error of reconstructions in the bimodal and unimodal model and the average relative sensitivity of ten different line pairs are also displayed in Table 1.

Obviously, different errors of reconstruction correlate with different relative sensitivities of the selected spectrum, so we then studied the relationship between the rel-

T a b l e 1. Spectroscopic parameters of ten selected spectra at 296 K including the information of wavelength, line strength, and lower state energy and the average relative sensitivity corresponding to the average error of the temperature reconstruction of the bimodal and unimodal model of these ten selected spectra.

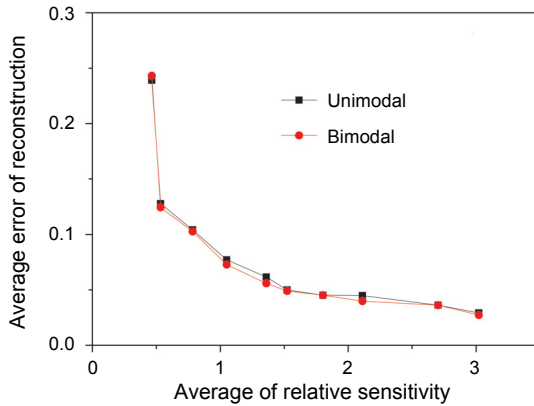| Line pairs	Wavelength [cm^{-1}]	Line strength (296 K) ×10^{-3} [cm^{-2}/atm]	Lower state energy ×10^3 [cm^{-1}]	Average of relative sensitivity	Average error of reconstruction	
					Unimodal model	Bimodal model
1	7169.8	0.022	2.4004	3.02	2.9%	2.7%
	7170.3	34.200	0.4196			
2	7160.2	132.100	0.2647	2.70	3.6%	3.6%
	7160.8	0.084	2.0376			
3	7159.2	0.154	1.6509	2.11	4.5%	4.0%
	7160.2	132.100	0.2657			
4	7164.9	3.500	1.4227	1.80	4.5%	4.5%
	7165.8	150.300	0.2375			
5	7153.4	0.004	2.7850	1.52	5.0%	4.9%
	7154.8	0.416	1.7866			
6	7164.9	3.500	1.4227	1.36	6.2%	5.6%
	7165.2	15.500	0.5402			
7	7202.9	125.100	0.0941	1.05	7.7%	7.3%
	7203.9	71.800	0.7791			
8	7190.7	0.696	1.5031	0.78	10.4%	10.3%
	7191.1	0.030	2.0167			
9	7202.3	27.800	0.4613	0.53	17.6%	18.1%
	7202.9	124.500	0.1117			
10	7165.2	15.500	0.5498	0.46	23.9%	24.3%
	7165.8	150.300	0.2375			

Fig. 7. The relationship between the average of relative sensitivity and the error of reconstruction.

ative sensitivity and the error of reconstruction from the simulated results of ten different spectra as shown in Fig. 7.

In Fig. 7, not all the error is reducing rapidly with an increase in the relative sensitivity value. When the relative sensitivity reaches a certain limit, the curve begins to change gently and the error reaches a steady value. As it is shown in Fig. 7, the relation curve has a critical corner (approximate in the 1.5), and all the error is reducing rapidly with an increase in the relative sensitivity value on the left of the corner. Due to the error in the algorithm, further increase in the relative sensitivity cannot sharply improve the quality of reconstruction, but in this range of the relative sensitivity from 1.5 to 3 the MATRT algorithm provides the high agreement between the reconstruction and the phantom.

The similar critical point would be recommended for selecting the average of relative sensitivity of the spectra larger than 1.5 in the production procedure of temperature reconstruction. We usually select the spectra beyond 1, but we can see from Fig. 7 that selecting the average of sensitivity much larger than 1 will reduce the errors effectively. The algorithm itself inevitably has a certain error, however, by selecting great relative sensitivity spectra within the wanted reconstruction temperature range, the temperature reconstruction errors can be reduced effectively.

6. Conclusions

The two-dimensional temperature reconstruction was realized by combining the MAART with TDLAS and using a two-wavelength scheme in this study. Considering that the temperature reconstructions can capture the shape and magnitude of two phantoms of H_2O distribution quite accurately in the range from 600 to 1400 K using the incomplete projections, the effectiveness of the MAART method and the corresponding LOS system were verified using numerical simulations. The program and the method described here have feasibility and are promising for practical temperature reconstruction in a combustion diagnosis.

Although the MAART with the TDLAS technique has workability in temperature reconstruction, the deviation of reconstructions from the phantoms still exists. So, extra simulations were carried out to study how various spectra of relative sensitivity influence the errors in temperature reconstruction. From the relationship between the reconstruction errors of unimodal and bimodal models, and the relative sensitivity of ten different spectra, the accuracy of temperature reconstruction can be improved by selecting the spectrum which has the higher relative sensitivity of the overall level. The critical corner values in the relation curve of relative sensitivity and error reconstruction will be beneficial in selecting the spectrum which would be practicable in temperature reconstruction for a propulsion combustion diagnosis. While a more accurate research concerning the best relative sensitivity in selecting the spectrum for effectively reducing the error reconstruction and experimental results would still be needed.

References

[1] LIU J.T., RIEKER G.B., JEFFRIES J.B., GRUBER M.R., CARTER C.D., MATHUR T., HANSON R.K., *Near-infrared diode laser absorption diagnostic for temperature and water vapor in a scramjet combustor*, Applied Optics **44**(31), 2005, pp. 6701–6711.

[2] TINGDONG CAI, GUISHI WANG, ZHENSONG CAO, WEIJUN ZHANG, XIAOMING GAO, *Sensor for headspace pressure and H_2O concentration measurements in closed vials by tunable diode laser absorption spectroscopy*, Optics and Lasers in Engineering **58**, 2014, pp. 48–53.

[3] TINGDONG CAI, GUANGZHEN GAO, YING LIU, *Calibration-free sensor for pressure and H_2O concentration in headspace of sterile vial using tunable diode laser absorption spectroscopy*, Applied Optics **52**(32), 2013, pp. 7682–7688.

[4] NICOLAS J.-C., BARANOV A.N., CUMINAL Y., ROUILLARD Y., ALIBERT C., *Tunable diode laser absorption spectroscopy of carbon monoxide around 2.35 µm*, Applied Optics **37**(33), 1998, pp. 7906–7911.

[5] MILLER M.F., KESSLER W.J., ALLEN M.G., *Diode laser-based air mass flux sensor for subsonic aeropropulsion inlets*, Applied Optics **35**(24), 1996, pp. 4905–4912.

[6] WANG F., CEN K.F., LI N., JEFFRIES J.B., HUANG Q.X., YAN J.H., CHI Y., *Two-dimensional tomography for gas concentration and temperature distributions based on tunable diode laser absorption spectroscopy*, Measurement Science and Technology **21**(4), 2010, article 045301.

[7] SATO M., NOMURA D., KITANO T., TSUNENARI T., NISHIDATE I., *Variations in signal intensity with periodical temperature changes in vivo in rat brain: analysis using wide-field optical coherence tomography*, Applied Optics **51**(10), 2012, pp. 1436–1445.

[8] XINLIANG AN, KRAETSCHMER T., TAKAMI K., SANDERS S.T., LIN MA, WEIWEI CAI, XUESONG LI, ROY S., GORD J.R., *Validation of temperature imaging by H_2O absorption spectroscopy using hyperspectral tomography in controlled experiments*, Applied Optics **50**(4), 2011, pp. A29–A37.

[9] BROWN M.S., HERRING G.C., CABELL K., HASS N., BARHORST T.F., GRUBER M., *Optical measurements at the combustor exit of the HIFiRE 2 ground test engine*, 50th AIAA Aerospace Sciences Meeting Including the New Horizons Forum and Aerospace Exposition, 2012.

[10] WRIGHT P., GARCIA-STEWART C.A., CAREY S.J., HINDLE F.P., PEGRUM S.H., COLBOURNE S.M., TURNER P.J., HURR W.J., LITT T.J., MURRAY S.C., CROSSLEY S.D., OZANYAN K.B., MCCANN H., *Toward in-cylinder absorption tomography in a production engine*, Applied Optics **44**(31), 2005, pp. 6578–6592.

[11] TERZIJA N., DAVIDSON J.L., GARCIA-STEWART C.A., WRIGHT P., OZANYAN K.B., PEGRUM S., LITT T.J., MCCANN H., *Image optimization for chemical species tomography with an irregular and sparse beam array*, Measurement Science and Technology **19**(9), 2008, article 094007.

[12] WEIWEI CAI, C.F. KAMINSKI, *Multiplexed absorption tomography with calibration-free wavelength modulation spectroscopy*, Applied Physics Letters **104**(15), 2014, article 154106.

[13] LIN MA, XUESONG LI, SANDERS S.T., CASWELL A.W., ROY S., PLEMMONS D.H., GORD J.R., *50-kHz-rate 2D imaging of temperature and H_2O concentration at the exhaust plane of a J85 engine using hyperspectral tomography*, Optics Express **21**(1), 2013, pp. 1152–1162.

[14] LIN MA, WEIWEI CAI, CASWELL A.W., KRAETSCHMER T., SANDERS S.T., ROY S., GORD J.R., *Tomographic imaging of temperature and chemical species based on hyperspectral absorption spectroscopy*, Optics Express **17**(10), 2009, pp. 8602–8613.

[15] JUNLING SONG, YANJI HONG, GUANGYU WANG, HU PAN, *Algebraic tomographic reconstruction of two-dimensional gas temperature based on tunable diode laser absorption spectroscopy*, Applied Physics B **112**(4), 2013, pp. 529–537.

[16] XIN ZHOU, XIANG LIU, JEFFRIES J.B., HANSON R.K., *Selection of NIR H_2O absorption transitions for in-cylinder measurement of temperature in IC engines*, Measurement Science and Technology **16**(12), 2005, pp. 2437–2445.

[17] ALLEN M.G., *Diode laser absorption sensors for gas-dynamic and combustion flows*, Measurement Science and Technology **9**(4), 1998, pp. 545–562.

[18] XIN ZHOU, XIANG LIU, JEFFRIES J.B., HANSON R.K., *Development of a sensor for temperature and water concentration in combustion gases using a single tunable diode laser*, Measurement Science and Technology **14**(8), 2003, pp. 1459–1468.

[19] BRYNER E., SHARMA M., GOYNE C., MCDANIEL J., SNYDER M., KRAUSS R., MARTIN E., DISKIN G., *Tunable diode laser absorption technique development for determination of spatially resolved water concentration and temperature*, 48th AIAA Aerospace Sciences Meeting Including the New Horizons Forum and Aerospace Exposition, Odando, USA: AIAA, 2010, pp. 1–299.

[20] NING LI, CHUNSHENG WENG, *Modified adaptive algebraic tomographic reconstruction of gas distribution from incomplete projection by a two-wavelength absorption scheme*, Chinese Optics Letters **9**(6), 2011, article 061201.

[21] SANE A., SATIJA A., LUCHT R.P., GORE J.P., *Simultaneous CO concentration and temperature measurements using tunable diode laser absorption spectroscopy near 2.3 μm*, Applied Physics B **117**(1), 2014, pp. 7–18.

[22] SHAO J., LATHDAVONG L., KLUCZYNSKI P., LUNDQVIST S., AXNER O., *Methodology for temperature measurements in water vapor using wavelength-modulation tunable diode laser absorption spectrometry in the telecom C-band*, Applied Physics B **97**(3), 2009, pp. 727–748.

[23] HANSEN P.C., SAXILD-HANSEN M., *AIR tools – a MATLAB package of algebraic iterative reconstruction methods*, Journal of Computational and Applied Mathematics **236**(8), 2012, pp. 2167–2178.

[24] GORDON R., BENDER R., HERMAN G.T., *Algebraic reconstruction techniques (ART) for three-dimensional electron microscopy and X-ray photography*, Journal of Theoretical Biology **29**(3), 1970, pp. 471–476.

[25] SAXILD-HANSEN M., *AIR Tools – A MATLAB Package for Algebraic Iterative Reconstruction Techniques*, Master's Thesis, Technical University of Denmark, DTU, DK-2800 Kgs. Lyngby, Denmark, 2010.

[26] DEZHONG WANG, TIANGE ZHUANG, *The measurement of 3-D asymmetric temperature field by using real time laser interferometric tomography*, Optics and Lasers in Engineering **36**(3), 2001, pp. 289–297.

[27] WEIWEI CAI, LIN MA, *Hyperspectral tomography based on proper orthogonal decomposition as motivated by imaging diagnostics of unsteady reactive flows*, Applied Optics **49**(4), 2010, pp. 601–610.
[28] ABBAS M., MAJID A.A., ALI J.M., *Positivity-preserving rational bi-cubic spline interpolation for 3D positive data*, Applied Mathematics and Computation **234**, 2014, pp. 460–476.
[29] LIN MA, WEIWEI CAI, *Numerical investigation of hyperspectral tomography for simultaneous temperature and concentration imaging*, Applied Optics **47**(21), 2008, pp. 3751–3759.